

Supplemental Material 1: ^{36}Cl Modeling

Content: This supplement contains additional information concerning the modeling of ^{36}Cl , that is 1) theoretical cosmogenic nuclides buildup on facet spurs 2) topographic shielding calculation for normal fault facet, 3) a series of sensitivity tests to assess the impact of the various parameters on the final theoretical ^{36}Cl concentration profile on a facet and 4) all details concerning the Bayesian inversion.

1) Cosmogenic nuclides buildup on facet spurs

In absence of denudation, the concentration of ^{36}Cl in a rock varies as a function of rock exposure time (t) and burial depth (z), as

$$dN(z, t)/dt = P_{36Cl}(z, t) - \lambda N(z, t) \quad (\text{Eq. 1.1})$$

where N is the number of atoms of ^{36}Cl , P_{36Cl} is the ^{36}Cl isotope production rate, λ is the decay constant of ^{36}Cl , and dN/dt is the rate of change.

This allows deriving the amount of ^{36}Cl accumulating over a certain period T at any depth z :

In our case, the total ^{36}Cl accumulated is the sum of ^{36}Cl accumulated during the long-term and progressive exhumation of the sample, and ^{36}Cl accumulated during the post glacial period exposure at the surface of the facet:

$$N_{36Cl} = \int_0^{T_{exhum}} P_{36Cl}(z(t)) \times \frac{(1-e^{-\lambda dt})}{\lambda} + \int_0^{T_{pg}} P_{36Cl}(z=0) \times \frac{(1-e^{-\lambda dt})}{\lambda} \quad (\text{Eq. 1.2})$$

with T_{exhum} , the exposition duration during which the sample has been progressively exhumed, and T_{pg} , the post-glacial period duration during which the sample has been exposed at the surface of the facet ($z=0$).

According to Schlagenhauf et al. 2010, the total ^{36}Cl production rate for a preserved rock sample can be calculated:

$$P_{36Cl}(z, t) = P(z) \times S(t) \times F(z) \times Q + P_{rad} \quad (\text{Eq. 1.3})$$

$P(z)$ is the sample-specific ^{36}Cl production rate modulated by the sample chemical composition and the sample depth, and P_{rad} is the radiogenic production. S, F and Q are scaling factors : S accounts for elevation, latitude and geomagnetic field and its potential variation with time (ref), F accounts for the corrections related to the shielding effects (topographic, geometric and cover shielding) which includes all parameters related to the fault facet geometry, and Q accounts for the sample thickness (Gosse & Philipps (2001)).

Following Tucker et al. (2011) and considering that the denudation-rate remains roughly constant over the time period considered, the successive positions $z(t)$ of any sample is controlled by the slip-rate of the fault (SR) as follows :

$$z(t_i) = z(t_{i-1}) + SR \times dt \quad (\text{Eq. 1.4})$$

2) Shielding factor equations for a facet

A correction of the ^{36}Cl production rate is required to account for the shielding of cosmic rays, produced by of the surrounding topography. According to Gosse & Philipps (2001) and references there in, the geometrical shielding factor for a sample at depth is computed integrating cosmic ray coming from the whole sky hemisphere, as follow:

$$F = \frac{m+1}{2\pi} \cdot \int_{\varphi=0}^{2\pi} \int_{\theta=0}^{\pi/2} \sin^m(\theta) \cos(\theta) \exp\left(-\frac{D \cdot \rho}{\Lambda}\right) d\phi d\theta \quad (\text{Eq. 2.1})$$

where m is the cosmic ray angular distribution, θ is the azimuth angle of the considered cosmic ray, ϕ is the inclination angle of the considered cosmic ray, D is the thickness of the crossed material in the direction (θ, ϕ) , ρ is the density of the material (g/cm^3), Λ is the true particle attenuation length (g/cm^2).

In the case of a normal fault-facet, cosmic rays will penetrate through colluvial wedge + some bedrock (case 1 in Fig. 2.1) to reach the rock sample localized at depth or only through bedrock (case 2 in Fig. 2.1).

For case 2, the geometrical shielding factor is expressed as follow:

$$F = \frac{m+1}{2\pi} \cdot \int_{\varphi=0}^{2\pi} \int_{\theta_{\min}}^{\pi/2} \sin^m(\theta) \cos(\theta) \exp\left(-\frac{D_1 \cdot \rho_{\text{rock}}}{\Lambda}\right) d\theta d\varphi \quad (\text{Eq. 2.2})$$

With D_1 the thickness (cm) of the bedrock crossed by a given cosmic ray (θ, φ) , ρ_{rock} the density of the footwall bedrock (g/cm^3), θ_{\min} the minimum incidence angle considered. For the upslope part, θ_{\min} is taken as the slope of the facet projected in the φ direction, giving $\theta_{\min} = \text{atan}(\tan(\gamma) \cdot \sin(\varphi))$. For the downslope part, θ_{\min} is taken as the incidence angle projected in the φ direction above which the cosmic rays are no more attenuated by the colluvial wedge, $\theta_{\min} = \text{atan}(\tan(\theta_{\text{coll}}) \cdot \sin(\varphi))$.

The thickness D_1 of the bedrock crossed by a given cosmic ray (θ, φ) is:

$$D_1 = \frac{Z \cdot \sin(\beta - \gamma)}{\sin(\theta) \cdot \cos(\gamma) - \sin(\gamma) \cdot \cos(\theta) \cdot \sin(\varphi)} \quad (\text{Eq. 2.3})$$

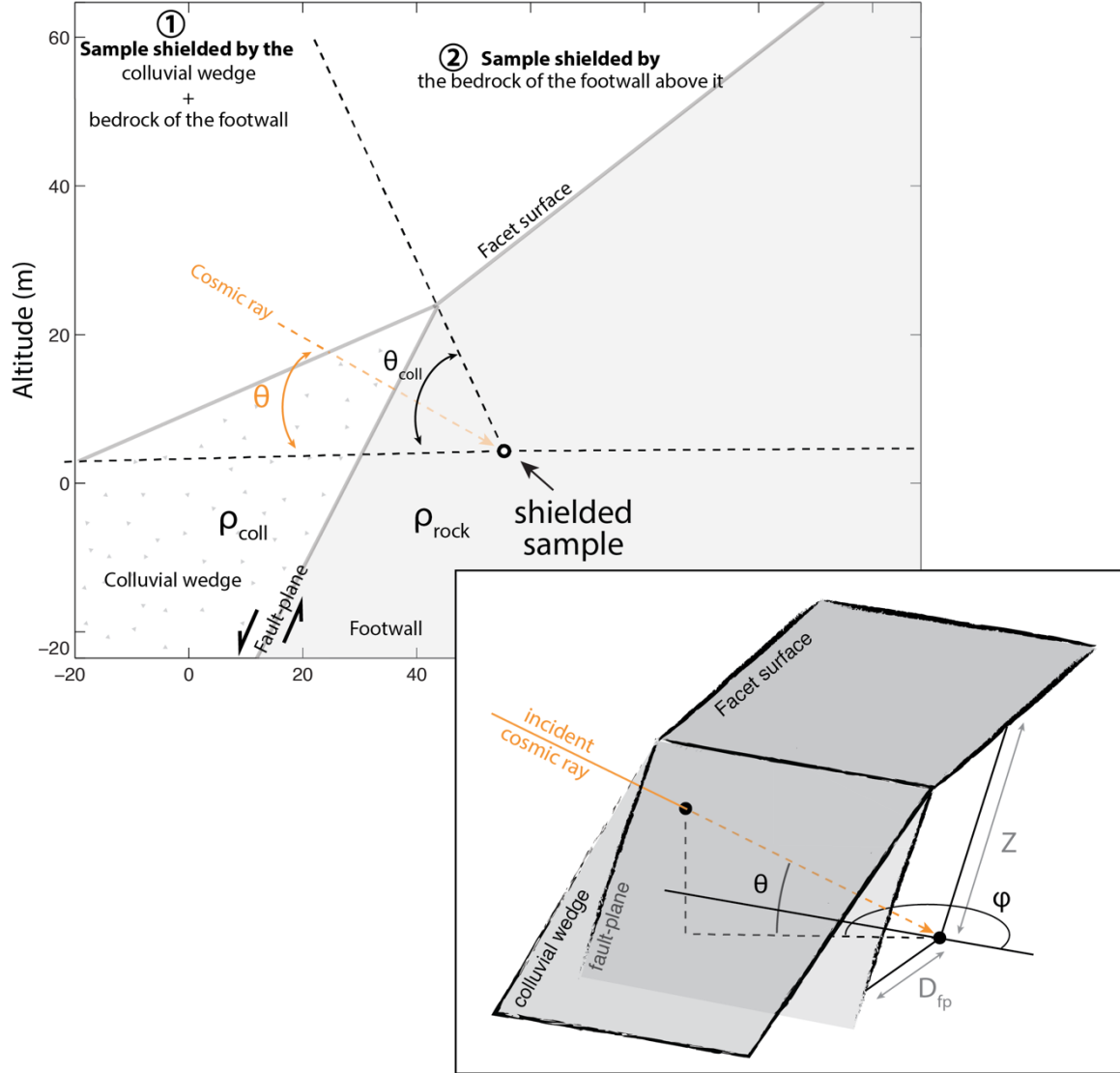


Figure 2.1: Shielding of cosmic ray for samples belonging to the fault footwall. According to Gosse and Philipps, (2001), the total cosmic ray flux reaching a sample is obtained by integration over the whole half-hemisphere. Depending on the location of the sample and on the cosmic ray incidence angle, cosmic ray may be attenuated by the presence of a colluvial wedge, and by the bedrock directly in front of or above the sample. The attenuation of a given cosmic ray (characterized by its inclination angle θ , and its azimuth φ), is computed after the thickness of colluvial wedge (d_{coll}) and the thickness of the bedrock (d_{rock}) crossed by the ray. The position of the sample is characterized by Z , the depth of the sample from the facet surface, and D_{fp} , the horizontal distance between

the fault-plane and the sample. θ_{coll} is the incidence angle above which the cosmic rays are not attenuated by the colluvial wedge.

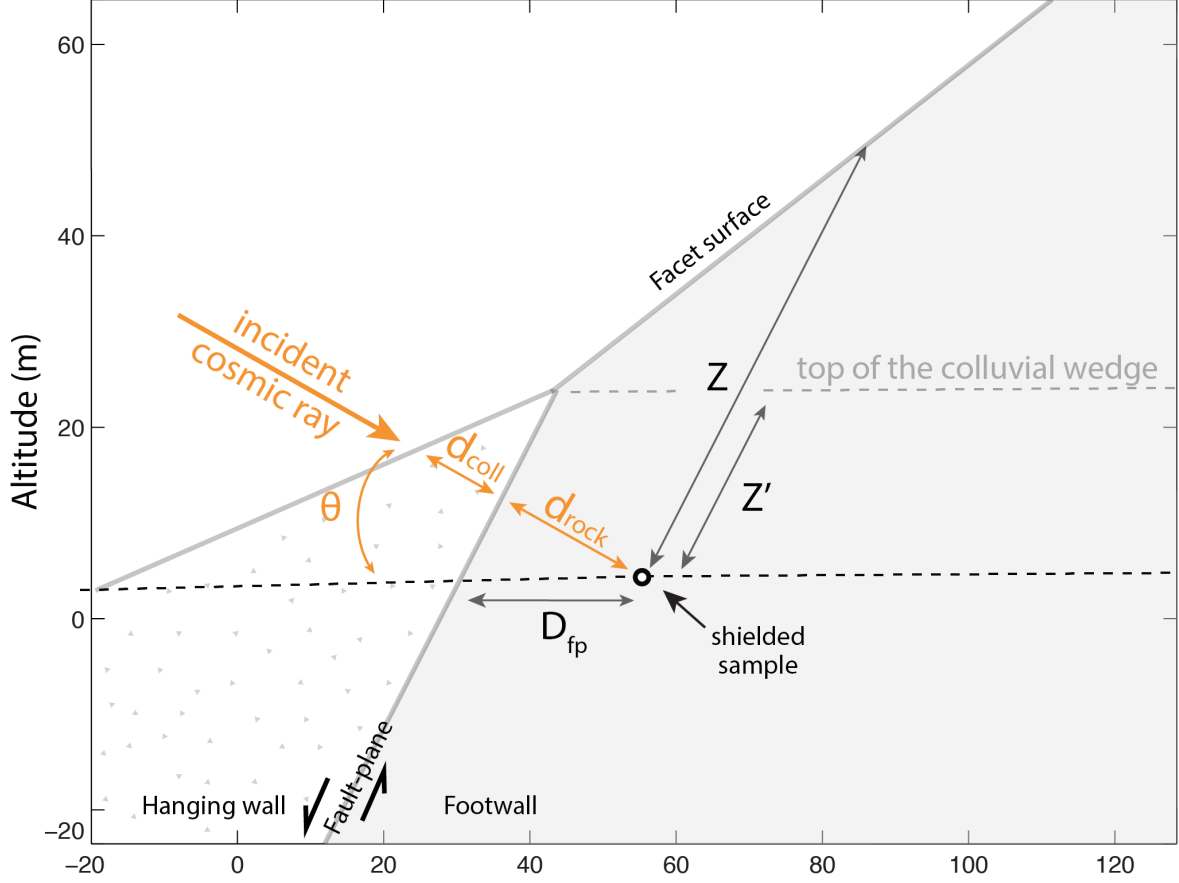


Figure 2.2: Geometric parameters used to compute cosmic ray attenuation through rock and colluvial wedge. The position of the sample is characterized by Z , the depth of the sample from the facet surface in the direction parallel to the fault-plane, Z' , the depth of the sample taken from the altitude of the colluvial wedge top, and D_{fp} , the horizontal distance between the fault-plane and the sample. The attenuation of a given cosmic ray (characterized by its inclination angle θ , and its azimuth φ), is computed after the thickness of colluvial wedge (d_{coll}) and the thickness of the rock (d_{rock}) crossed by the ray.

For case 1, the geometrical shielding factor is expressed as follow:

$$F = \frac{m+1}{2\pi} \cdot \int_{\varphi=0}^{2\pi} \int_{\theta=0}^{\theta_{max}} \sin^m(\theta) \cos(\theta) \exp\left(-\frac{D_2 \cdot \rho_{coll} + D_3 \cdot \rho_{rock}}{\Lambda}\right) d\theta d\varphi \quad (\text{Eq. 2.4})$$

With D_2 the thickness (cm) of the colluvial wedge crossed by a given cosmic ray (θ, φ), D_3 the thickness (cm) of the rock crossed by a given cosmic ray (θ, φ), ρ_{rock} the density of the footwall rock (g/cm^3), ρ_{coll} the density of the colluvial wedge (g/cm^3), and θ_{min} is the minimum incidence angle considered. For the downslope part, θ_{max} is taken as the incidence angle projected in the φ direction, above which the cosmic rays are no more attenuated by the colluvial wedge, $\theta_{\text{max}} = \text{atan}(\tan(\theta_{\text{coll}}) \cdot \sin(\varphi))$.

The thickness D_2 of the portion of colluvial wedge crossed by a given cosmic ray (θ, φ) is:

$$D_2 = \frac{Z' \cdot \sin(\beta - \alpha) + A \cdot \sin(\alpha)}{\sin(\theta) \cdot \cos(\alpha) - \sin(\alpha) \cdot \cos(\theta) \cdot \sin(\varphi)} - \frac{Dfp \cdot \sin(\beta)}{\sin(\theta) \cdot \cos(\beta) - \sin(\beta) \cdot \cos(\theta) \cdot \sin(\varphi)} \quad (\text{Eq. 2.5})$$

The thickness D_3 of the rock crossed by a given cosmic ray (θ, φ) is:

$$D_3 = \frac{Dfp \cdot \sin(\beta)}{\sin(\theta) \cdot \cos(\beta) - \sin(\beta) \cdot \cos(\theta) \cdot \sin(\varphi)} \quad (\text{Eq. 2.6})$$

3) Sensitivity test

Several tests are presented to assess the sensitivity of the model to the main parameters affecting ^{36}Cl concentration profiles on a facet. For each test, theoretical $[^{36}\text{Cl}]$ have been computed for samples located all along the height of a 300 m high surface facet. The geometric characteristic of the site are colluvial wedge surface slope $\alpha = 25^\circ$, a fault-plane dip $\beta = 55^\circ$, and a fault-plane surface slope $\gamma = 30^\circ$. The density of footwall rock is 2.6 g/cm^3 , the density of the colluvial wedge is 1.6 g/cm^3 . Samples are progressively exhumed during $T_{\text{exhum}} = 300 \text{ kyr}$ at the fault slip-rate 1 mm/yr , reaching the surface of the facet at $T_{\text{pg}} = 18 \text{ ka}$.

a. Testing variable fault slip-rate

The Fig 3.1 shows $[^{36}\text{Cl}]$ profiles for slip-rate varying between 0.1 to 2.0 mm/yr . A slip-rate of 2 mm/yr gives $[^{36}\text{Cl}]$ 2 times lower ($0.7 - 0.9 \times 10^6 \text{ at. of } ^{36}\text{Cl/ gr of rock}$) than for a slip-rate of 0.1 mm/yr ($1.4 \text{ to } 1.7 \times 10^6 \text{ at. of } ^{36}\text{Cl/ gr of rock}$). Small variations ($0.1 \times 10^6 \text{ at. of } ^{36}\text{Cl/ gr of rock}$) are observed between $[^{36}\text{Cl}]$ profiles with 1 mm/yr and 2 mm/yr . The $[^{36}\text{Cl}]$ variation can

be quite significant between 0.1 and 1 mm/yr, and smaller for higher slip-rate. This implies that the resolution of the method might be greater for relatively low slip-rate (0.1-0.5 mm/yr), than for relatively high slip-rate (0.5-2 mm/yr).

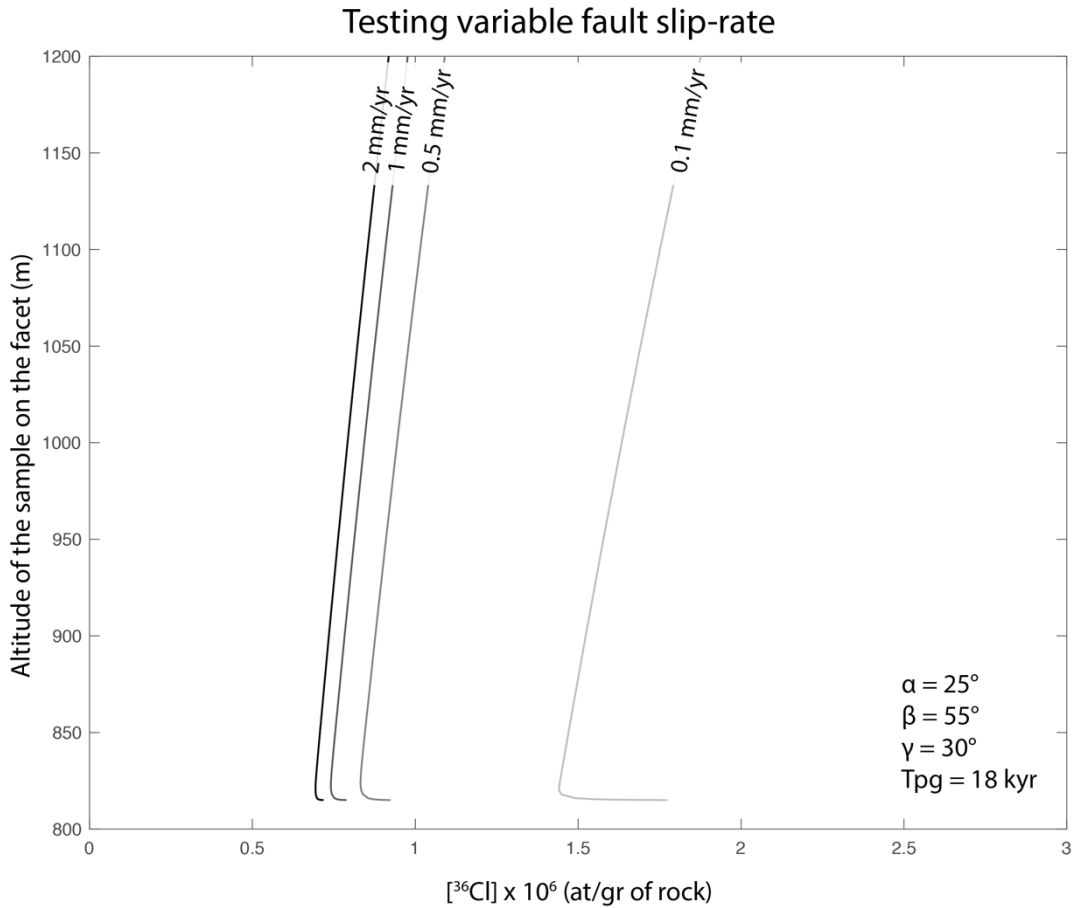


Figure 3.1: Sensibility of $[^{36}\text{Cl}]$ modeled on the facet surface, to the fault slip-rate. Samples are progressively exhumed during 300 kyr at the fault slip-rate (0.1, 0.5, 1, 2 mm/yr), reaching the surface of the facet at $T_{pg} = 18$ ka.

b. Testing variable post-glacial exposure duration (T_{pg})

The Fig 3.2 shows $[^{36}\text{Cl}]$ profiles for post-glacial exposure duration (T_{pg}) varying between 15 kyr to 25 kyr. A T_{pg} of 25 kyr gives ^{36}Cl concentrations 2x higher (around $1.0 - 1.2 \times 10^6$ at. of $^{36}\text{Cl}/\text{gr}$ of rock) than a T_{pg} of 10 kyr (0.5 to 0.6×10^6 at. of $^{36}\text{Cl}/\text{gr}$ of rock). A variation of 5 kyr on T_{pg} , results in 20-30% of variation on the final ^{36}Cl concentrations. Those results suggest that the $[^{36}\text{Cl}]$ profiles significantly varies depending on the post-glacial duration.

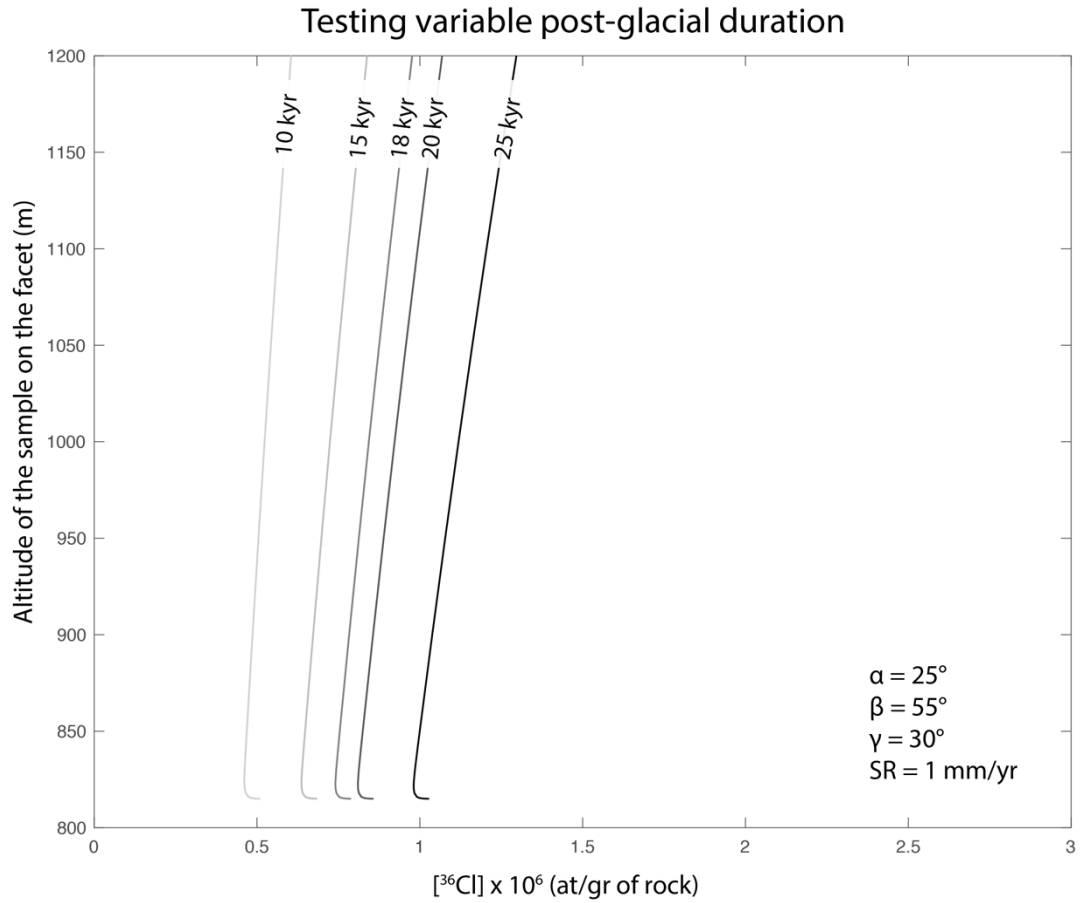


Figure 3.2: Sensibility of $[^{36}\text{Cl}]$ modeled on the facet surface, to the post-glacial period duration (T_{pg}). The samples are progressively exhumed during 300 kyr at fault slip-rate of $SR = 1 \text{ mm/yr}$, reaching the surface of the facet at variable T_{pg} (10, 15, 18, 20, 25 ka).

c. Testing variable colluvial wedge slope

Fig 3.3 shows $[^{36}\text{Cl}]$ profiles for variable slope for the colluvial wedge slope (α) between 20° to 50° . The fault slip-rate is 1 mm/yr and the post-glacial duration is 18 kyr. Considering a 55° dipping fault-plane (β), it gives $\alpha - \beta$ values ranging from 5° , representing a thin colluvial wedge, to 35° , representing a thick colluvial wedge. $[^{36}\text{Cl}]$ profiles are similar, except for the bottom samples that exhibits higher $[^{36}\text{Cl}]$ as the thickness of the colluvial wedge decreases. For thin colluvial wedge ($\alpha - \beta = 5^\circ$), $[^{36}\text{Cl}]$ at the bottom of the profile are around $1.2 \times 10^6 \text{ at. of } ^{36}\text{Cl/ gr of rock}$, while for thick colluvial wedge ($\alpha - \beta = 35^\circ$) $[^{36}\text{Cl}]$ are around $0.7 \times 10^6 \text{ at. of } ^{36}\text{Cl/ gr of rock}$. Those results suggest that the slope of the colluvial wedge (α), or its thickness, may partly control the $[^{36}\text{Cl}]$ at the bottom of the profile with variations up to 60 %. Steep and thin colluvial wedge tends to promotes large increase of $[^{36}\text{Cl}]$ at the bottom of the facet.

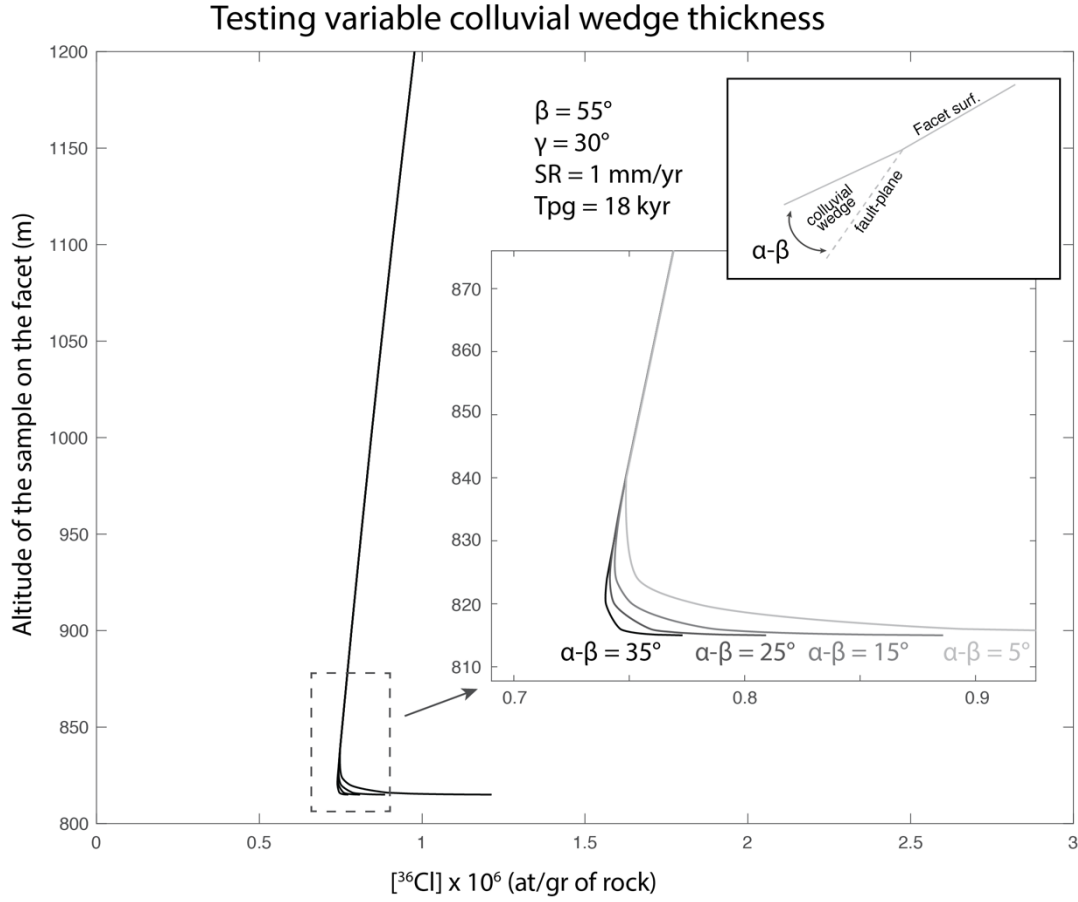


Figure 3.3: Sensibility of $[^{36}\text{Cl}]$ modeled on the facet surface, to the colluvial wedge thickness. Site characteristics are variable colluvial wedge surface slope with $\alpha = 20, 30, 40, 50^\circ$, $\beta = 55^\circ$, $\gamma = 30^\circ$. Thickness of the colluvial wedge can be assessed by the $\alpha - \beta$ value. The higher $\alpha - \beta$, the thicker the colluvial wedge and the greater the cosmic ray attenuation.

d. Testing variable fault-plane dipping

Fig. 3.4 shows $[^{36}\text{Cl}]$ profiles for variable fault plane dipping angle (θ) between 40° to 70° . The fault slip-rate is 1 mm/yr and post-glacial duration is 18 kyr. The difference observed between the $[^{36}\text{Cl}]$ profiles are around $0.05 - 0.3 \times 10^6$ at. of ^{36}Cl /gr of rock, constant all along the height of the facet. For θ values commonly observed, around $50-60^\circ$, we observe that 10° of variation results in less than 10% of variation on the total $[^{36}\text{Cl}]$.

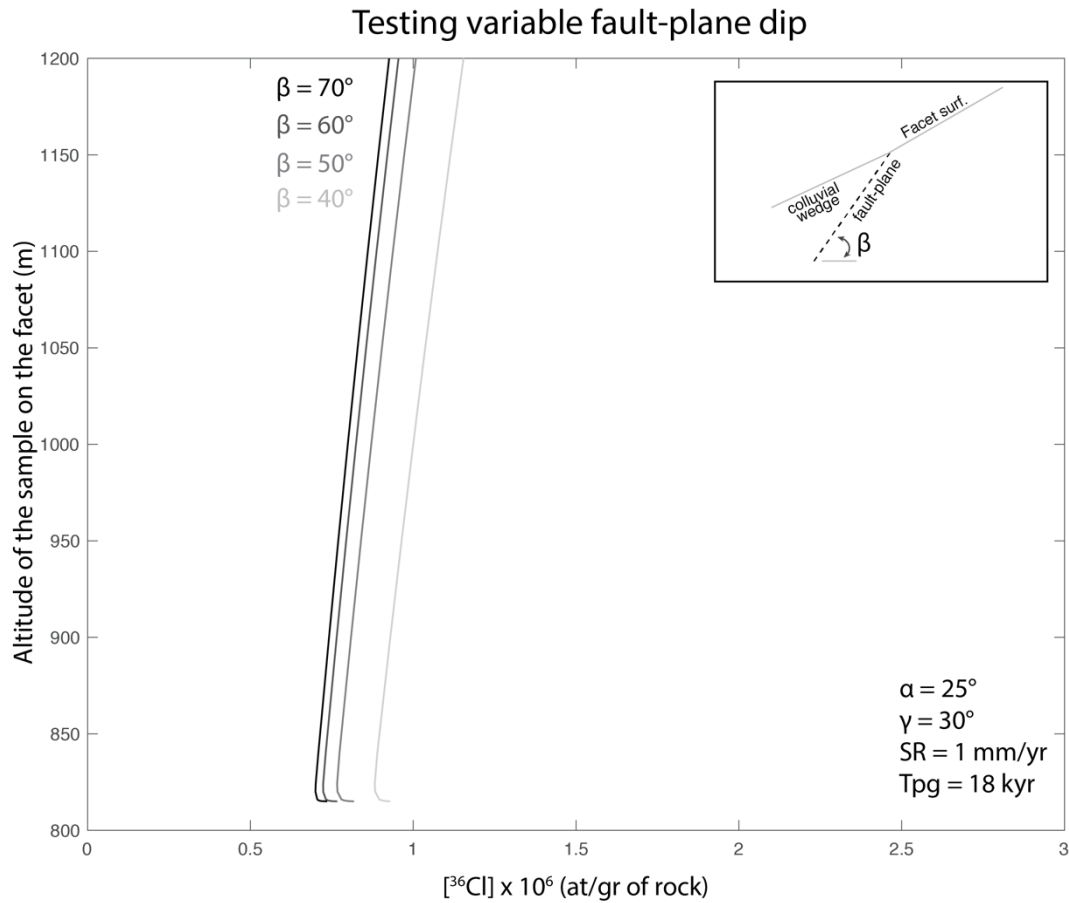


Figure 3.4: Sensibility of $[^{36}\text{Cl}]$ modeled on the facet surface, to the fault plane dip (β). The morphology of the normal fault escarpment is characterized by a colluvial wedge surface slope $\alpha = 25^\circ$, a fault-plane dip $\beta = 40, 50, 60, 70^\circ$, and a fault-plane surface slope $\gamma = 30^\circ$.

e. Testing variable facet surface slope

The Fig. 3.5 shows $[^{36}\text{Cl}]$ profiles for facet slope (γ) varying between 10° to 50° . The slip-rate of the fault is 1 mm/yr and the post-glacial duration is 18 kyr. For facet slope ranging between 10° and 40° , the $[^{36}\text{Cl}]$ profiles are quite similar with variation of 0.1×10^6 at. of ^{36}Cl / gr of rock between the profiles, representing ~10-15% of the total concentration. For larger slope ($\gamma=50^\circ$), the difference with lower slope reaches 0.2×10^6 at. of ^{36}Cl / gr of rock. If considering regular facet slope around 30° , a variation of 10° will results in 7% of variation on the $[^{36}\text{Cl}]$.

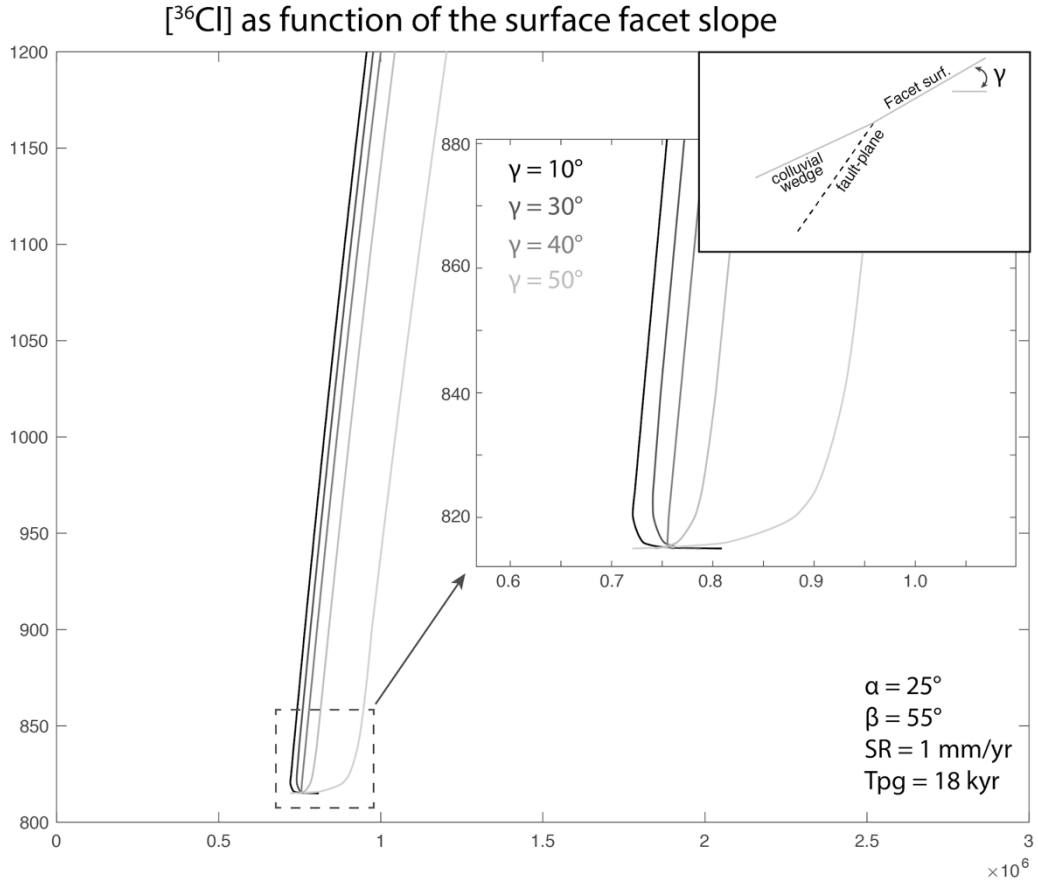


Figure 3.5: Sensibility of $[^{36}\text{Cl}]$ modeled on the facet surface, to the colluvial wedge density (γ). The morphology of the normal fault escarpment is characterized by a colluvial wedge surface slope $\alpha = 25^\circ$, a fault-plane dip $\beta = 55^\circ$, and a fault-plane surface slope $\gamma = 10^\circ, 20^\circ, 30^\circ, 40^\circ, 50^\circ$.

f. Testing variable colluvial wedge density

The Fig. 3.6 shows $[^{36}\text{Cl}]$ profiles for a density of the colluvial wedge of 1.0 and 2.0 g/cm³. The slip-rate of the fault is 1 mm/yr and the post-glacial duration is 18 kyr. The two $[^{36}\text{Cl}]$ profiles are similar with values ranging between 0.7-0.9 at. of ^{36}Cl / gr of rock, except at the very bottom where a difference of 0.04 at. of ^{36}Cl / gr of rock (~5%) is observed between the two profiles. A lowered density of the colluvial wedge promotes higher $[^{36}\text{Cl}]$ close at the bottom of the facet. A variation of 0.5 g/cm³ on the colluvial wedge density, results in 3% of variation on the $[^{36}\text{Cl}]$.

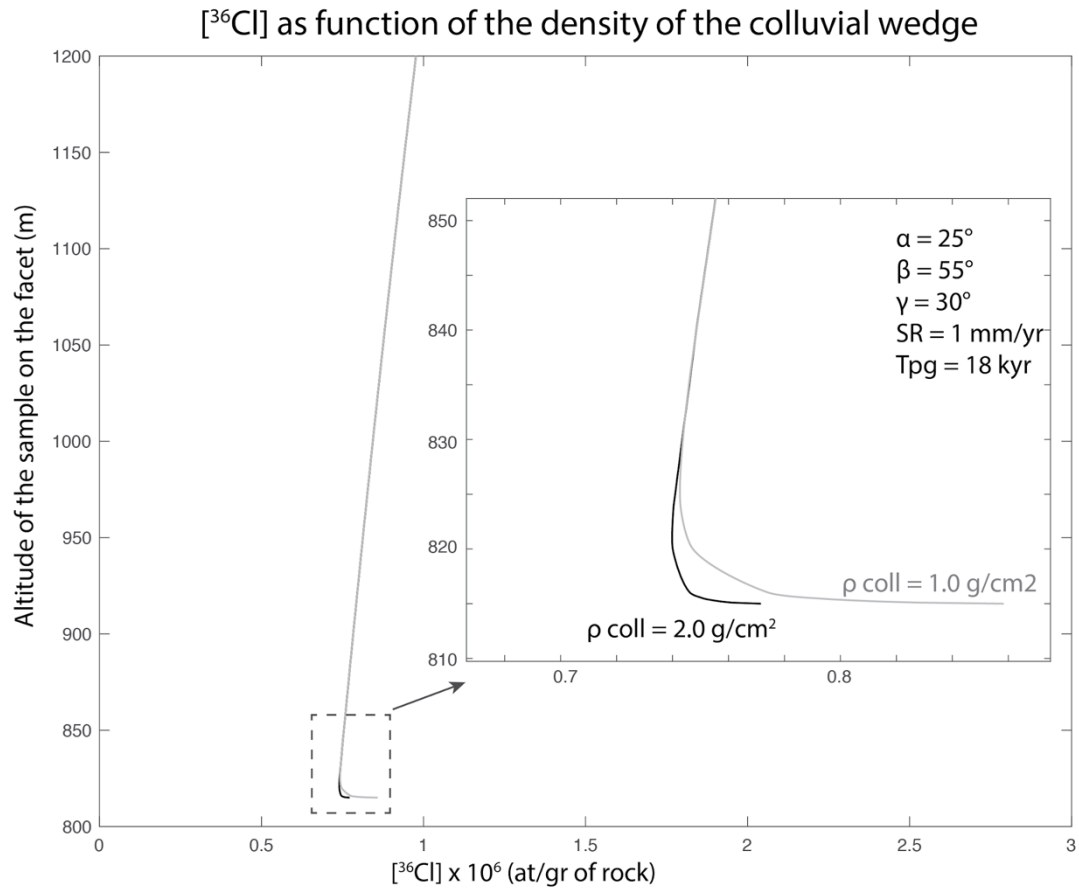


Figure 3.6: Sensibility of $[^{36}\text{Cl}]$ modeled on the facet surface, to the colluvial wedge density (ρ_{coll}). The density of footwall rock is 2.6 g/cm^2 , the density of the colluvial wedge is $\rho_{coll} = 1.0, 2.0 \text{ g/cm}^2$.

g. Testing variable scree cover

We test the effect of a scree cover on the facet surface (Table 3.1). The modeled $[^{36}\text{Cl}]$ profiles have been generated for each site with a scree thickness of 5, 10, 30, 50, 100 cm. and compared with the model resulting from the inversion at each site assuming no scree cover. Results are presented in Table 3.1. Scree cover mostly yields a decrease in production rate, and thus in the $[^{36}\text{Cl}]$ from few percent for a scree cover of 5-10 cm thick, to about 80 % for ≈ 100 cm thick. Only at MA3 a scree cover of less than 5-10 cm yields an increase in $[^{36}\text{Cl}]$. This situation is promoted by a relatively large slip-rate (3 mm/yr), and some samples that bears high natural chlorine concentration $[\text{Cl}] > 50 \text{ ppm}$. This favors ^{36}Cl production through epithermal and thermal reactions maximized at depth between 0 and 100 cm (e.g. Schimmelpfennig et al. 2009).

Table 3.1: Mean variation between modeled [36Cl] profiles with no scree cover and with 5, 10, 30, 50 and 100 cm thick. The density for the scree cover used for the modeling is 1.5 g/cm²

Scree cover thickness	5 cm	10 cm	20 cm	30 cm	50 cm	100 cm
MA3	+ 7 %	+ 4 %	- 8 %	- 8 %	- 35 %	- 59 %
MA1	- 1 %	- 4 %	- 13 %	- 21 %	- 33 %	- 53 %
ARC	- 10 %	-19 %	- 37 %	-48 %	- 63 %	- 80 %
BAZ	- 4 %	-13 %	- 31 %	- 44 %	- 60 %	- 76 %

4) Bayesian inversion of ³⁶Cl data from normal fault facet

a. Bayesian inference

Bayesian inference aims at quantifying the *a posteriori* probability distribution of the model parameters, m , given the observed data, d_{obs} , noted as $p(d_{obs})$. Following Baye's rule, the posterior distribution is deduced from the combination of the model structure $p(d_{obs}/m)$ and the prior $p(m)$:

$$posterior \propto likelihood \times prior \quad (4.1)$$

$$p(d_{obs}) \propto p(d_{obs}/m)p(m) \quad (4.2)$$

where the likelihood function $p(d_{obs}/m)$, is the probability that the model reproduces the observed data given the model m . The prior $p(m)$ is the probability of the set of parameters m , representing our knowledge of m before performing the inference.

The posterior distribution thus represents how our prior knowledge of parameters m is able to reproduce data.

Posterior distributions are constructed by sampling the parameter space in such a way that the sampling density of each parameter reflects that of the posterior distribution. To infer the

model parameters, we used the Goodman and Weare Markov chain Monte Carlo (GW-McMC, Goodman and Weare 2010) sampler based on the Metropolis-Hasting algorithm (Metropolis et al., 1953; Hastings, 1970). The GW-McMC use affine invariant methods that significantly speed up the inversion, compared with standard McMC algorithm. This algorithm use several “walkers” that perform random walk in the parameter space. The particularity of GW-McMC is that the proposal moves for each walker are generated using the distribution of other walkers in the ensemble. Similarly to standard McMC algorithm, the proposed moves are either accepted or rejected following an acceptance criterion. If the move is accepted, the new position represents one iteration for the walker, and the whole process is repeated. If the model is rejected, the walker remains in the same position, representing also one iteration. To ensure the models are statistically independent from each other, one model every 10th are effectively retained in the final ensemble. After an initial period (“burn-in” period) during which the random walkers progressively moves toward low misfit region(s), the chain is assumed to be stationary, meaning the parameter space tends to be sampled according to the **posterior probability distribution**. After a sufficient number of iterations, the ensemble of models (excluding the burn-in period, generally the first 20% models) might thus provide a good approximation of the posterior distribution for the model parameters.

b. **Model parameterization**

i. **Single site case**

For the inversion of a single site, the model parameters m to be inverted are, the slip-rate of the fault (SR), and the post-glacial period duration (T_{pg}) during which samples are directly exposed at the surface of the facet (considering denudation is null). Conversely the duration of the long-term exhumation of the samples before reaching the surface (T_{exhum}) is fixed a priori and estimated from the height of the facet and an estimate of the fault slip-rate. For instance for a fault that exhibits 300 m high facet and an estimated slip-rate of 1 mm/yr, we will assume a $T_{exhum} = 300$ kyr. The model to be inverted is $m = [SR, T_{pg}]$.

ii. **Multi-site case**

If dealing with several sites located in the same area, it can be supposed that all sites has encountered the same climate change, thus a similar post-glacial period duration (T_{pg}). Inversing the data from all sites together would thus allow to better constrain T_{pg} , and at the

same time the slip-rate of each fault. In such case, the model parameters m to be inverted are, the slip-rate of the n faults (SR_1, SR_2, \dots, SR_n), and the common post-glacial period duration (Tpg). The model to be inverted is $m = [SR_1, SR_2, \dots, SR_n, Tpg]$.

c. The forward model

Testing a model m of exhumation requires computing the ^{36}Cl concentration that would theoretically be observed within each sample of the facet(s) using a forward model. We have improved the Modelscarp model previously initially proposed by Schlagenhauf et al. (2010) in order to speed up the theoretical ^{36}Cl concentration calculation, and include:

- 1) facet-specific shielding factors.
- 2) include 3 geomagnetic databases:
 - Atmospheric ^{10}Be -based VDM (0-60 ka: Muscheler et al. (2005); 60-2000 ka: SINT2000 (Valet et al., 2005))
 - Lifton VDM 2016 (0-14 ka: Pavon-Carrasco et al. (2014); 14-75 ka: GLOPIS-75 (Laj et al., 2004); 75-2000 ka: PADM2M (Ziegler et al., 2011))
 - LSD Framework (Lifton et al., 2014)
- 3) include both the Lal/Stone time dependent scaling model (Lal, 1991 ; Stone, 2000) and the LSD model (Lifton et al., 2014),
- 4) include the standard atmosphere pressure, and the ERA40 atmosphere model.

The latest muon production calculation from Heisinger (2002a and b) implemented by Balco et al. (2008 and 2017), cannot be used here because the integration of muon energy in the case of a complex geometry such as a facet requires additional development that has not been achieved now. In detail, this requires computing the different angular dependence for each energy from the surface energy spectrum, and then propagating downward using numerical integration. Instead the muon production rate is approximated with a single exponential function with a constant attenuation length of 1500 g/cm^2 . This approach does not correctly approximate the muon flux and in particular the increase of the muon energy with depth resulting in an increase of the instantaneous attenuation length with depth (see details in Balco, 2017).

In addition, facet-specific shielding factors are distinctly computed for neutronic and muonic reactions, using their respective attenuation length, 160 g/cm² and 1510 g/cm². This ensures that muons are not under-estimated at greater depth.

d. The likelihood function

The likelihood function $p(d_{obs}/m)$ provides the probability of a tested scenario using the common Gaussian-based expression:

$$p(d_{obs}|m) = \prod_{i=1}^N \left(\frac{1}{\sqrt{(2\pi)\sigma_i}} \right) \exp \left[-\frac{\chi^2(m)}{2} \right] \quad (4.3)$$

Where χ^2 is a weighted sum of squared residuals (WSSR) for a given model m , and σ_i is the ³⁶Cl measured uncertainties.

The weighted sum of squared residuals is calculated with the following expression:

$$\chi^2(m) = \sum_{i=1}^N \left(\frac{d_i - g(m)_i}{\sigma_i} \right)^2 \quad (4.4)$$

Where d_i is the measured ³⁶Cl of the sample i , and $g(m)_i$ is the modeled ³⁶Cl.

For numerical stability, it is, however, often preferable to work with the log-likelihood function, $l(d_{obs}/m)$, instead of $p(d_{obs}/m)$:

$$l(d_{obs}|m) = \ln [p(d_{obs}|m)] \quad (4.5)$$

e. The prior distribution

The prior probability $p(m)$ of the searched parameters is the *a priori* knowledge we have on certain parameters. The prior distribution should be rigorously chosen since it controls the final results (the posterior probability distribution). To reduce the influence of the prior, we set an uniform distribution for each searched parameter with large bounds, instead of a Gaussian density function centered on a particular value. In doing so, we allow the final results to be dominated by the data, not by the prior.

The prior distribution for the searched parameters are as presented below for all the tests presented in the following sections:

- fault(s) slip-rate ranges between 0 and 20 ka ($p(SR) = U(0,5 \text{ mm/yr})$),

- post-glacial period duration ($p(Tpg) = U(5,30 \text{ kyr})$).

f. The posterior distribution

Following the Bayesian formulation, the posterior distribution of all searched parameters is then written:

$$p(d_{obs}) \propto p(d_{obs} | k, a, s, sr) p(k) p(a) p(s) p(sr) \quad (4.6)$$

g. Assessing algorithm convergence

Algorithm convergence can be evaluated on the basis of the autocorrelation function plot that is automatically generated following the data inversion. User is also able to verify that the burnin period is long enough (usually 20% of the first iterations is removed). In the case of a multi-site inversion (4 sites, with a total of 30 samples), our tests suggest that 300 000 iterations with 10 walkers are required to provide statistically reliable posterior distribution. A minimum of 50 000 iteration is required to provide a rough estimation of the parameters values. Increasing the number of samples, and the number of sites will require more iterations.

h. Program performance

Our new modeling code greatly improve the time required to compute ^{36}Cl concentration. This program run under Matlab®, Octave® and can be easily used on a personal computer, since the time required to run the inversion spend from less than 1h to ~12h. The program also provide the possibility to get the theoretical ^{36}Cl concentration of a given model. This program is under GNU license, and available at: https://github.com/jimtesson/Facet_36Cl_CREp, with a tutorial to use it.

Suppl. 2 Sites data

Content:

Figures 1.1, 1.2 and 1.3 present the morphology of the sampled facet F-MA1, F-MA3, F-ARC and F-BAZ. Shaded digital elevation models have been produced using aerial stereographic photography, providing an horizontal resolution < 0.5 cm and a vertical resolution of 1 m.

The geometric characteristics of the sampled facet are presented in Tab. 1.1.

The geographic position of the collected samples are presented in Tab. 1.2.

All samples have been chemically prepared at CEREGE, Aix en Provence, following the chemical procedure described in Stone et al. (1996) and adapted as in Schlagenhauf et al. (2010). Cl and ^{36}Cl were then measured by accelerator mass spectrometry (AMS) at the French AMS national facility ASTER, housed at CEREGE, Aix en Provence, France. [Cl] was determined by isotope dilution accelerator mass spectrometry at ASTER (Bouchez et al., 2015). Both the $^{36}\text{Cl}/^{35}\text{Cl}$ and the $^{35}\text{Cl}/^{37}\text{Cl}$ ratios were standardized against the in-house standard SM-CL-12 with an assigned $^{36}\text{Cl}/^{35}\text{Cl}$ value of $(1.428 \pm 0.021) \times 10^{-12}$ (Merchel et al., 2011), and assuming a natural $^{35}\text{Cl}/^{37}\text{Cl}$ ratio of 3.127. Analytical uncertainties (reported as 1s) include uncertainties associated with AMS counting statistics, chemical blank measurements, and AMS internal error (0.5%). All results are presented in Tab. 1.3. Major and trace elements were measured at SARM-CRPG (France) and presented in Tab. 1.4.

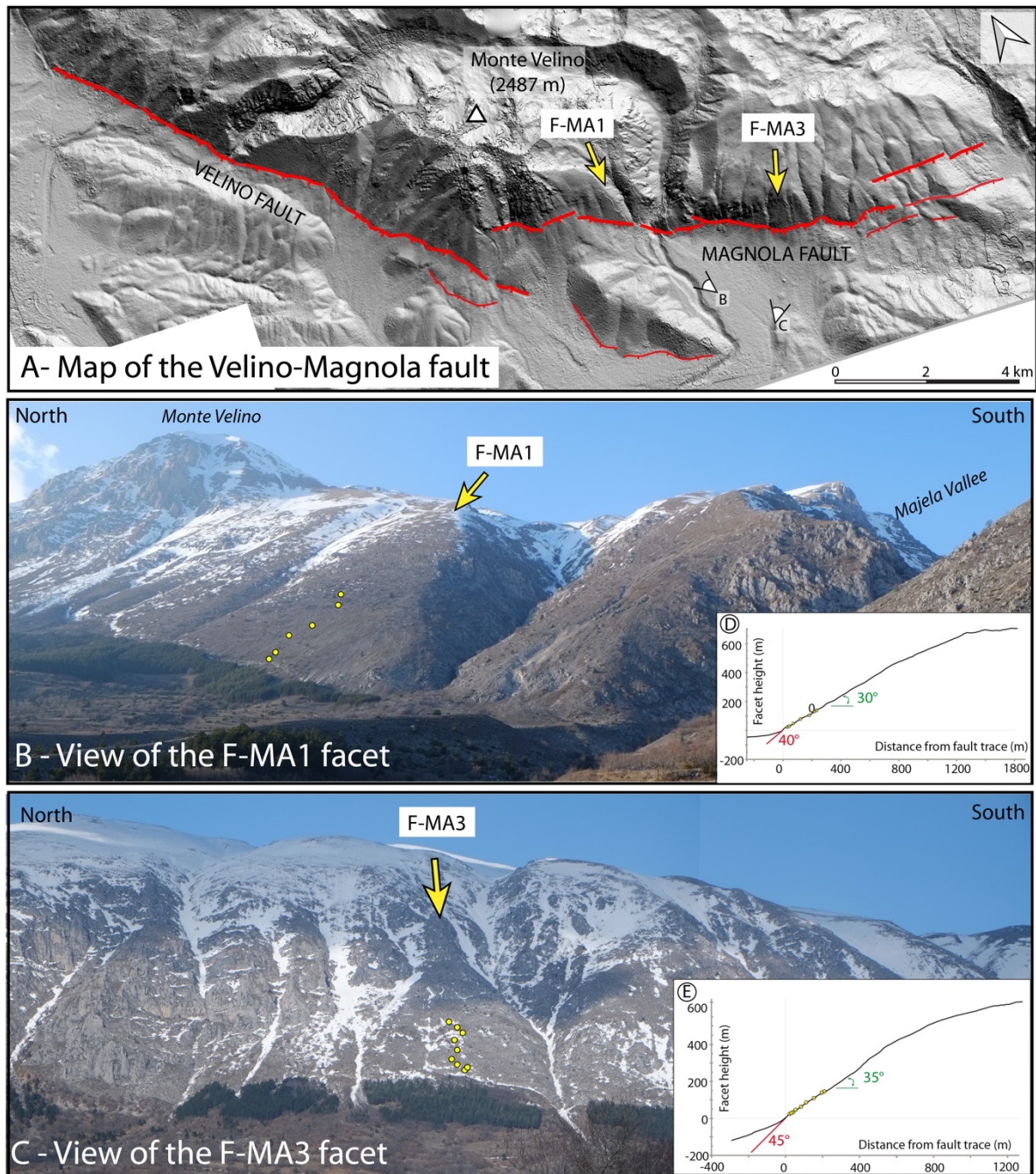


Fig 1.1 : Morphology of the Magnola fault facets (F-MA1 and F-MA3). A) Map of the Velino-Magnola fault (Schlagenhauf et al. 2011). Digital elevation model has been produced using aerial stereographic photography. B) Photography of the F-MA1 facet, C) Photography of the F-MA3 facet. D) and E) Topographic profiles of each facet with samples localization (yellow dots) and fault dip and facet slope.

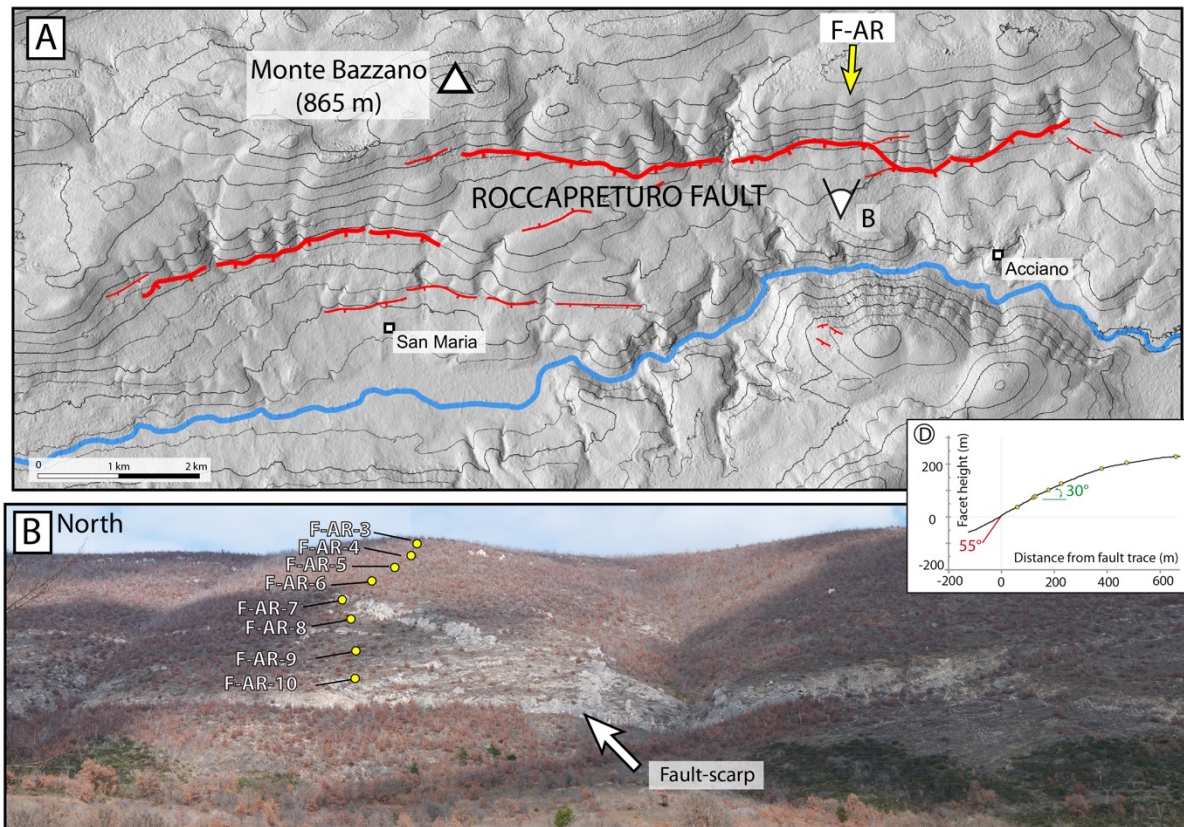


Fig 1.2 : Morphology of Roccapreturo fault facet (F-AR). A) Map of Roccapreturo fault (Tesson et al. 2017). Digital elevation model has been produced using aerial stereographic photography. B) Photography of F-AR facet. D) Topographic profile of the facet with samples localization (yellow dots) and fault dip and facet slope.

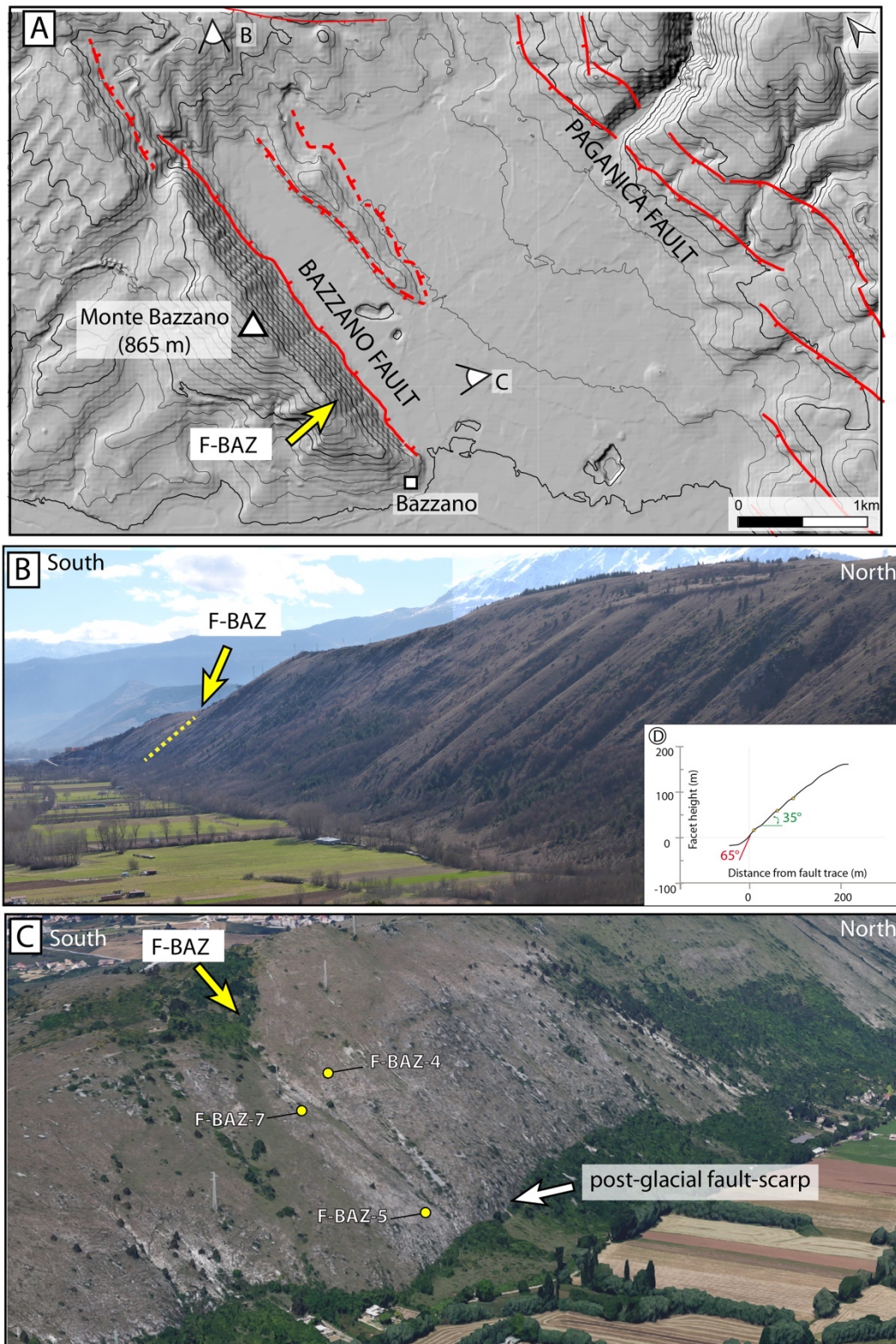


Fig 1.3 : Morphology of Bazzano fault facet (F-BAZ). A) Map of Bazzano fault (Tesson et al. 2017). Digital elevation model has been produced using aerial stereographic photography. B) Photography of Bazzano hillslope, C) Satellite imagery of the sampled Bazzano fault hillslope. D) Topographic profile of facet with samples localization (yellow dots) and fault dip and facet slope.



Fig 1.4 : Sampling at MA1 (A), MA3 (B), AR (C) and BAZ (D).

Table 1.1: Characteristics of the sampled normal fault facet surfaces in Central Appenines (Italy). Note that naming convention for the angles is according to Schlagenhauf et al. (2010) and differs from Tucker et al. (2011).

Site	MA3	MA1	ARC	BAZ
Fault-dip β (°)	45	40	55	65
Facet slope γ (°)	35	30	30	35
Colluvial wedge surface slope α (°)	30	25	25	25
Altitude of the post-glacial scarp top (m)	1275	1280	815	643

Table 1.2: Localization of the samples collected on the normal fault facet surface in Central Apennines (Italy)

Sample name	Latitude (°)	Longitude (°)	Altitude (m)
Magnola fault - Facet MA3			
F_MA3_1	N42.12178300	E13.44767150	1404
F_MA3_2	N42.12164817	E13.44783133	1393
F_MA3_3	N42.12146583	E13.44775330	1371
F_MA3_4	N42.12121600	E13.44737330	1350
F_MA3_5	N42.12097383	E13.44723583	1324
F_MA3_6	N42.12076500	E13.44706983	1314
F_MA3_7	N42.12048133	E13.44724300	1297
F_MA3_8	N42.12026683	E13.44704983	1281
F_MA3_9	N42.12055000	E13.44752717	1287
Magnola fault - Facet MA1			
F_MA1_1	N42.13023933	E13.41339450	1420
F_MA1_2	N42.1296525	E13.41337867	1416
F_MA1_3	N42.12964967	E13.41338130	1381
F_MA1_4	N42.12928383	E13.41297750	1357
F_MA1_5	N42.12859000	E13.41319050	1305
F_MA1_6	N42.12839933	E13.41318567	1302
Roccapreturo fault			
F_AR_3	N42.19464617	E13.71451233	1060
F_AR_4	N42.19399217	E13.71415133	1026
F_AR_5	N42.19368900	E13.71347717	996
F_AR_6	N42.19313360	E13.71283710	951
F_AR_7	N42.19276000	E13.71234000	917
F_AR_8	N42.19259000	E13.71223000	895
F_AR_9	N42.19233000	E13.71206000	888
F_AR_10	N42.19204000	E13.71165000	859

Bazzano fault

F_BAZ_4	N42.3437200	E13.4503000	644
F_BAZ_5	N42.3434400	E13.4488800	721
F_BAZ_7	N42.3429800	E13.4494100	710

Table 1.3: Mean chemical composition (^{36}Cl , natural chlorine and Calcium content) of the samples used for the modeling of ^{36}Cl concentrations. ^{36}Cl and natural chlorine are measured at the french AMS ASTER. The Calcium is measured using an ICP-MS.

Sample	[^{36}Cl]	$\sigma_{[^{36}\text{Cl}]}$	Cl_{nat} (ppm)	$\sigma_{[\text{Cl}]}$	Ca (%)
Magnola fault - Facet 1					
F_MA3_1	1.07E+06	3.46E+04	27.3	2.7	38.3
F_MA3_2	1.21E+06	4.02E+04	39.8	4.0	38.9
F_MA3_3	1.03E+06	3.55E+04	27.0	2.7	39.5
F_MA3_4	1.33E+06	4.38E+04	102.8	10.3	23.8
F_MA3_5	1.43E+06	4.82E+04	33.1	3.3	39.6
F_MA3_6	8.55E+05	2.80E+04	29.3	2.9	38.9
F_MA3_7	1.11E+06	3.81E+04	16.6	1.7	39.9
F_MA3_8	1.74E+06	5.58E+04	7.3	0.7	37.6
F_MA3_9	9.46E+05	3.15E+04	4.6	0.5	37.4
F_MA3_10	1.21E+06	3.90E+04	43.1	4.3	38.4
Magnola fault - Facet 2					
F_MA1_1	2.33E+06	7.65E+04	19.4	1.9	39.5
F_MA1_2	2.39E+06	7.46E+04	36.6	3.7	38.7
F_MA1_3	2.54E+06	7.90E+04	25.5	2.6	40.5
F_MA1_4	1.80E+06	5.69E+04	28.0	2.8	39.8
F_MA1_5	3.04E+06	8.42E+04	20.5	2.0	41.2
F_MA1_6	3.03E+06	8.35E+04	21.1	2.1	39.5
Roccapreturo fault					
F_AR_3	1.06E+06	2.93E+04	3.81	0.4	39.39
F_AR_4	1.05E+06	3.41E+04	3.32	0.3	39.74
F_AR_5	8.55E+05	2.63E+04	5.58	0.6	39.12
F_AR_6	9.99E+05	2.91E+04	5.51	0.6	39.16
F_AR_7	1.14E+06	3.45E+04	5.55	0.6	39.67
F_AR_8	8.75E+05	2.69E+04	12.79	1.3	39.57
F_AR_9	8.20E+05	2.60E+04	18.23	1.8	37.52

F_AR_10	1.40E+06	4.15E+04	35.19	3.5	39.18
Bazano fault					
F_BAZ_4	1.34E+06	4.56E+04	60.14	6.0	39.22
F_BAZ_5	2.55E+06	9.39E+04	91.08	6.9	35.83
F_BAZ_7	2.14E+06	7.40E+04	69.25	9.1	39.96

Table 1.4: Mean chemical composition of the samples used in the modeling of ^{36}Cl concentration. The composition used for the MA1 facet is taken from the MA1 fault plane in Schlagenhauf et al. 2010, the MA3 facet composition is taken from the MA3 fault plane in Schlagenhauf et al. 2010. The composition used for the BAZ samples and the ARC samples is the mean composition of the post-glacial fault-plane measured just below each facet.

	As (ppm)	Ba (ppm)	Be (ppm)	Bi (ppm)	Cd (ppm)	Ce (ppm)	Co (ppm)	Cr (ppm)	Cs (ppm)
MA1	0.000	4.847	0.037	0.000	0.324	0.361	1.984	0.337	0.013
MA3	0.000	3.082	0.000	0.000	0.268	0.526	2.115	0.000	0.000
BAZ	0.000	3.082	0.000	0.000	0.268	0.526	2.115	0.000	0.000
AR	0.183	3.887	0.000	0.000	0.203	0.516	1.132	0.000	0.000

	Cu (ppm)	Dy (ppm)	Er (ppm)	Eu (ppm)	Ga (ppm)	Gd (ppm)	Ge (ppm)	Hf (ppm)	Ho (ppm)
MA1	0.000	0.097	0.078	0.017	0.000	0.080	0.000	0.004	0.024
MA3	0.000	0.123	0.086	0.024	0.000	0.111	0.000	0.000	0.028
BAZ	0.000	0.123	0.086	0.024	0.000	0.111	0.000	0.000	0.028
AR	2.089	0.129	0.088	0.027	0.000	0.120	0.000	0.002	0.030

	In (ppm)	La (ppm)	Lu (ppm)	Mo (ppm)	Nb (ppm)	Nd (ppm)	Ni (ppm)	Pb (ppm)	Pr (ppm)
MA1	0.000	0.572	0.012	0.000	0.008	0.342	21.187	49.416	0.080
MA3	0.000	0.649	0.013	0.000	0.000	0.474	21.523	5.346	0.114
BAZ	0.000	0.648	0.013	0.000	0.000	0.474	21.523	5.346	0.114
AR	0.000	1.257	0.013	0.000	0.010	0.616	8.094	0.618	0.150

	Rb (ppm)	Sb (ppm)	Sm (ppm)	Sn (ppm)	Sr (ppm)	Ta (ppm)	Tb (ppm)	Th (ppm)	Tm (ppm)
MA1	0.100	0.000	0.068	0.000	183.12 2	0.000	0.013	0.009	0.011
MA3	0.387	0.000	0.097	0.000	116.05 0	0.000	0.018	0.038	0.013

BAZ	0.387	0.000	0.096	0.000	116.05 0	0.000	0.018	0.038	0.013
AR	0.426	0.000	0.111	0.000	282.94 7	0.000	0.018	0.038	0.012

	U (ppm)	V (ppm)	W (ppm)	Y (ppm)	Yb (ppm)	Zn (ppm)	Zr (ppm)	SiO ₂ (%)	Al ₂ O ₃ (%)
MA1	0.351	1.221	0.000	1.524	0.073	0.000	0.179	0.000	0.015
MA3	0.311	0.000	0.000	1.372	0.081	0.000	0.000	0.000	0.031
BAZ	0.311	0.000	0.000	1.372	0.081	0.000	0.000	0.000	0.031
AR	0.482	2.361	0.000	1.569	0.080	7.584	0.000	0.000	0.036

	Fe ₂ O ₃ (%)	MnO (%)	MgO (%)	CaO (%)	Na ₂ O (%)	K ₂ O (%)	TiO ₂ (%)	P ₂ O ₅ (%)	B (ppm)
MA1	0.000	0.001	0.549	54.818	0.000	0.000	0.001	0.007	1.000
MA3	0.000	0.004	0.390	55.368	0.000	0.000	0.000	0.034	2.000
BAZ	0.000	0.004	0.390	54.521	0.000	0.000	0.000	0.034	2.000
AR	0.010	0.002	0.384	55.453	0.000	0.000	0.000	0.029	2.133

	Li (ppm)	H ₂ O (%)	S (%)	CO ₂ (%)	O _{rock} (%)	O _{water} (%)
MA1	0.811	0.560	0.016	44.249	0.000	0.000
MA3	0.919	0.288	0.015	43.850	0.000	0.000
BAZ	0.919	0.288	0.015	43.850	0.000	0.000
AR	1.027	0.305	0.021	43.949	0.000	0.000

Cited References

Balco, G., Stone, J. O., Lifton, N. A., & Dunai, T. J. (2008). A complete and easily accessible means of calculating surface exposure ages or erosion rates from ¹⁰Be and ²⁶Al measurements. *Quaternary geochronology*, 3(3), 174-195.

Balco, G. (2017). Production rate calculations for cosmic-ray-muon-produced ^{10}Be and ^{26}Al benchmarked against geological calibration data. *Quaternary Geochronology*, 39, 150-173.

Bouchez, C., Pupier, J., Benedetti, L., Deschamps, P., Guillou, V., Keddadouche, K., ... & Bourlès, D. (2015). Isotope Dilution-AMS technique for ^{36}Cl and Cl determination in low chlorine content waters. *Chemical Geology*, 404, 62-70.

Goodman, J., & Weare, J. (2010). Ensemble samplers with affine invariance. *Communications in applied mathematics and computational science*, 5(1), 65-80.

Gosse, J. C., & Phillips, F. M. (2001). Terrestrial in situ cosmogenic nuclides: theory and application. *Quaternary Science Reviews*, 20(14), 1475-1560.

Heisinger, B., Lal, D., Jull, A. T., Kubik, P., Ivy-Ochs, S., Neumaier, S., ... & Nolte, E. (2002). Production of selected cosmogenic radionuclides by muons: 1. Fast muons. *Earth and Planetary Science Letters*, 200(3-4), 345-355.

Heisinger, B., Lal, D., Jull, A. T., Kubik, P., Ivy-Ochs, S., Knie, K., & Nolte, E. (2002). Production of selected cosmogenic radionuclides by muons: 2. Capture of negative muons. *Earth and Planetary Science Letters*, 200(3-4), 357-369.

Laj, C., Kissel, C., & Beer, J. (2004). High resolution global paleointensity stack since 75 kyr (GLOPIS-75) calibrated to absolute values. Washington DC American Geophysical Union Geophysical Monograph Series, 145, 255-265.

Lal, D. (1991). Cosmic ray labeling of erosion surfaces: in situ nuclide production rates and erosion models. *Earth and Planetary Science Letters*, 104(2-4), 424-439.

Stone, J. O. (2000). Air pressure and cosmogenic isotope production. *Journal of Geophysical Research: Solid Earth*, 105(B10), 23753-23759.

Lifton, N., Sato, T., & Dunai, T. J. (2014). Scaling in situ cosmogenic nuclide production rates using analytical approximations to atmospheric cosmic-ray fluxes. *Earth and Planetary Science Letters*, 386, 149-160.

Merchel, S., Bremser, W., Alfimov, V., Arnold, M., Aumaître, G., Benedetti, L., ... & Freeman, S. P. H. T. (2011). Ultra-trace analysis of ^{36}Cl by accelerator mass spectrometry: an interlaboratory study. *Analytical and bioanalytical chemistry*, 400(9), 3125-3132.

Muscheler, R., Beer, J., Kubik, P. W., & Synal, H. A. (2005). Geomagnetic field intensity during the last 60,000 years based on ^{10}Be and ^{36}Cl from the Summit ice cores and ^{14}C . *Quaternary Science Reviews*, 24(16-17), 1849-1860.

Pavón-Carrasco, F. J., Osete, M. L., Torta, J. M., & De Santis, A. (2014). A geomagnetic field model for the Holocene based on archaeomagnetic and lava flow data. *Earth and Planetary Science Letters*, 388, 98-109.

Schimmelpfennig, I., Benedetti, L., Finkel, R., Pik, R., Blard, P. H., Bourles, D., ... & Williams, A. (2009). Sources of in-situ ^{36}Cl in basaltic rocks. Implications for calibration of production rates. *Quaternary Geochronology*, 4(6), 441-461.

Schlagenhauf, A., Gaudemer, Y., Benedetti, L., Manighetti, I., Palumbo, L., Schimmelpfennig, I., ... & Pou, K. (2010). Using in situ Chlorine-36 cosmonuclide to recover past earthquake histories on limestone normal fault scarps: a reappraisal of methodology and interpretations. *Geophysical Journal International*, 182(1), 36-72.

Stone, J. O., Allan, G. L., Fifield, L. K., & Cresswell, R. G. (1996). Cosmogenic chlorine-36 from calcium spallation. *Geochimica et Cosmochimica Acta*, 60(4), 679-692.

Tucker, G. E., McCoy, S. W., Whittaker, A. C., Roberts, G. P., Lancaster, S. T., & Phillips, R. (2011). Geomorphic significance of postglacial bedrock scarps on normal-fault footwalls. *Journal of Geophysical Research: Earth Surface*, 116(F1).

Valet, J. P., Meynadier, L., & Guyodo, Y. (2005). Geomagnetic dipole strength and reversal rate over the past two million years. *Nature*, 435(7043), 802.

Ziegler, L. B., Constable, C. G., Johnson, C. L., & Tauxe, L. (2011). PADM2M: a penalized maximum likelihood model of the 0–2 Ma palaeomagnetic axial dipole moment. *Geophysical Journal International*, 184(3), 1069-1089.